Modeling long-term creep rupture by debonding in unidirectional fibre-reinforced composites

Boumediene Nedjar

Modeling long-term creep rupture by debonding in unidirectional fibre-reinforced composites

B. Nedjar[a,*]

[a] *Mechanical Engineering Unit, Materials and Structures group, ENSTA-ParisTech, 91762 Palaiseau, France*

Abstract

Delayed fracture due to debonding can be observed in many unidirectional fibre-reinforced composites when the fibre/matrix interface experiences creep. The aim of this work is to describe such a phenomenon within the recently proposed modeling framework of transverse isotropy that allows for a neat decomposition of the mechanical behavior into fibre-directional, transverse, and pure shear parts. Specifically, debonding is here chosen to be governed by the tension transverse to the fibres. One can then speak of a mode-I debonding if use is made of the terminology adopted in fracture mechanics. On another hand, the time-dependent response is attributed to the matrix constituent. As the role of this latter is to deform and support stresses primarily in shear, a viscoelastic behavior is introduced that affects solely the pure shear part of the behavior. We show that both characteristics can be easily embedded into the aforementioned formulation. Among others, the occurrence of tertiary creep is made possible to predict. It is otherwise found that the predicted debonding path always propagates along the direction of

*Corresponding author, phone: 33 1 69 31 98 15
Email address: boumediene.nedjar@ensta-paristech.fr (B. Nedjar)

the fibres in agreement with many experimental observations found in the literature. On the numerical side, the algorithmic treatment of debonding is independent of the one for viscoelasticity. This renders the implementation within the context of the finite element method very easy.
Keywords: Fibre-reinforced composites, Debonding, Viscoelastic matrix, Tertiary creep, Finite element method

---

1. Introduction

In general, debonding in unidirectional fibre-reinforced composites occurs locally at the interface between fibre and matrix, mostly when the interface is weak. As a consequence, this phenomenon can significantly reduce structural stiffness before eventual catastrophic failure. It is then of interest to build predictive modeling tools to ensure maximum security of the stuctures.

There has been extensive study of these composites in the literature. For instance, at the micro- and meso-scale levels, models based on extended versions of the shear-lag model to multi-fibre composites involving the interactions between the fibres and the matrix have been widely developed, see for example (Ochiai et al., 1999; Beyerlein and Landis, 1999), or more recently, models based on damage mechancis as well as elastoplasticity have been proposed that take into account the characteristic behavior of each component to represent their influence on the overall composite properties, see for example the recent references (Needleman et al., 2010; Kurnatowski and Matzenmiller, 2012; Nedjar et al., 2014).

In this work, a macroscale point of view is adopted where the fibres are considered to be continuously arranged throughout the material. The result-

ing composite exhibits then strong directional dependencies. Fibre/matrix debonding is here described by the concept of the plasticity theory which requires the introdution of a yield criterion together with companion flow rules that control the way dedonding takes place. It is then of importance to judiciously choose the aforementioned criterion. This task is drastically simplified by adopting the so-called integrity-basis formulation of transverse isotropy as proposed by Spencer (1984). This basis consists of invariants of the strain tensor together with invariants of tensor products of the strain with the structural tensor, the latter being the dyadic product of the fibres' direction, see also (Kaliske, 2000; Nedjar, 2011). Notice that the formalism of integrity-basis is nowadays widely employed in the finite strain range, among others, see for example (Weiss et al., 1996; Bonet and Burton, 1998; Holzapfel, 2000) for purely hyperelastic fibre-reinforced materials, and (Kaliske, 2000; Klinkel et al., 2005; Nedjar, 2007) for cases where, in addition, inelasticity can occur such like plasticity or viscoelasticity. In all cases, the formulation does not depend on a particular choice of coordinate system, *i.e.* it is not necessary that one of the coordinate axes coincides with the direction of the fibres.

Within this formulation, the stress-strain constitutive relation can be decomposed into fibre-directional, transverse, and pure shear parts. It is this fact that is exploited in the present modeling framework. On the one hand, the form adopted in this paper for the plastic yield criterion is chosen to depend on the tension transverse to the fibres, *i.e.* a mode-I debonding, and on the other hand, for the time-dependent part of the behavior, viscoelasticity is introduced that solely affects the pure shear part of the material

response. This latter has recently been developed in full detail in (Nedjar, 2011). Hence, the combination of the two processes allows to built a model that is able to capture short-term as well as long-term mode-I debonding phenomena.

The rest of the paper is organized as follows. The transversely isotropic formulation we use is recalled in Section 2 where the constitutive stress-strain decomposition is developed. Debonding modeling is motivated and developed in full detail in Section 3 where the combination with viscoelastic behavior of the matrix constituent is introduced as well. The numerical integration of the constitutive model and local evolution equations at hand is then detailed in Section 4 for an easy implementation within a finite element procedure. Then, a set of numerical examples is given in Section 5 where we show the effectiveness of the present framework. Finally, conclusions and perspectives are drawn in Section 6.

Notation: Throughout the paper, bold face characters refer to second- or fourth-order tensors. In particular, $\mathbf{1}$ denotes the second-order identity tensor with components δ_{ij}, $i,j=1,\ldots,n_{\text{dim}}$, δ_{ij} being the Kronecker delta and n_{dim} is the problem dimension, and $\boldsymbol{I}$ is the fourth-order unit tensor of components $I_{ijkl}=\frac{1}{2}(\delta_{ik}\delta_{jl}+\delta_{il}\delta_{jk})$. The double dot symbol ':' is used for double tensor contraction. In particular, one has the property $\text{tr}[(\boldsymbol{.})]=(\boldsymbol{.}):\mathbf{1}$ for the trace operator. The notation $\otimes$ stands for the tensorial product. In components, one has for any second order tensors $\boldsymbol{A}$ and $\boldsymbol{B}$, $(\boldsymbol{A}\otimes\boldsymbol{B})_{ijkl}=\boldsymbol{A}_{ij}\boldsymbol{B}_{kl}$, and for any vectors $\vec{U}$ and $\vec{V}$, $(\vec{U}\otimes\vec{V})_{ij}=U_iV_j$. Furthermore, the upper dot notation $(\dot{})$ always refers to the time derivative.

2. Transverse isotropy and stress-strain decompositions

Let denote by $\vec{V}$ the *unit* vector that characterizes the direction of the fibres. Its components V_i $(i = 1, 2, 3)$ with respect to a fixed global cartesian basis $\{\vec{e}_i\}_{i=1,2,3}$ is regarded as a continuous function of the position. In the same way, we also introduce the continuous tensor field of the micro-structure defined by the dyadic product $\boldsymbol{M} = \vec{V} \otimes \vec{V}$. Notice the useful property $\boldsymbol{M}^n = \boldsymbol{M}$ for any integer $n > 0$, *i.e.* $\boldsymbol{M}$ is idempotent.

In the most general case with one family of fibres, the integrity-basis is given by five irreductible invariants

$$I_1 = \mathrm{tr}[\boldsymbol{\varepsilon}] \quad I_2 = \boldsymbol{\varepsilon} : \boldsymbol{\varepsilon} \quad I_3 = \det[\boldsymbol{\varepsilon}] \quad I_4 = \boldsymbol{\varepsilon} : \boldsymbol{M} \quad I_5 = \boldsymbol{\varepsilon}^2 : \boldsymbol{M} \tag{1}$$

where $\boldsymbol{\varepsilon}$ is the infinitesimal strain tensor, $\det[\centerdot]$ designating the determinant operator. I_1, I_2 and I_3 are the classical invariants related to isotropy, and I_4 and I_5 reflect the presence of the family of fibres. In this section, only linear elasticity is of concern with a totally reversible strain tensor. The occurrence of plastic and viscous strainings will be considered later on in Section 3.

As the strain energy $\mathcal{W}$ is quadratic with respect to the strain tensor, it then becomes independent of the cubic invariant I_3. Its expression is given by, see (Spencer, 1984)

$$\mathcal{W} = \frac{1}{2}\lambda\, I_1^2 + \mu_T\, I_2 + \alpha\, I_1 I_4 + 2(\mu_L - \mu_T)\, I_5 + \frac{1}{2}\beta\, I_4^2 \tag{2}$$

where the five parameters λ, μ_T, μ_L, α and β are Lamé-like elastic constants, see also (Holzapfel, 2000; Kaliske, 2000; Nedjar, 2011, 2014) for details: μ_L and μ_T are the shear moduli on planes parallel to- and normal to- the fibres,

respectively, and λ, α and β can easily be related locally to the standard engineering parameters, see below.

As the stress tensor is given by the state law $\boldsymbol{\sigma} = \partial\mathcal{W}/\partial\boldsymbol{\varepsilon}$, the following linear stress-strain constitutive relation is obtained

$$\begin{aligned} \boldsymbol{\sigma} &= \lambda\,\mathrm{tr}[\boldsymbol{\varepsilon}]\,\mathbf{1} + \beta\,[\boldsymbol{\varepsilon}:\boldsymbol{M}]\,\boldsymbol{M} \\ &\quad +\alpha\left\{\mathrm{tr}[\boldsymbol{\varepsilon}]\boldsymbol{M} + [\boldsymbol{\varepsilon}:\boldsymbol{M}]\mathbf{1}\right\} \\ &\quad +2\,\mu_T\,\boldsymbol{\varepsilon} + 2(\mu_L - \mu_T)\left\{\boldsymbol{M}\boldsymbol{\varepsilon} + \boldsymbol{\varepsilon}\boldsymbol{M}\right\} \end{aligned} \tag{3}$$

In this form, there is no need to select a coordinate system $\{\vec{e}_i\}_{i=1,2,3}$ such that one of the coordinate axes coincides with the axis of transverse isotropy. The five elastic constants are related to the engineering parameters as

$$\begin{aligned} \mu_L &= G_{LT} \\ \mu_T &= \frac{E_T}{2(1+\nu)} \\ \lambda &= \frac{\nu E_L E_T + \nu_{LT}^2 E_T^2}{E_L(1-\nu^2) - 2E_T\nu_{LT}^2(1+\nu)} \\ \alpha &= \frac{(\nu_{LT} + \nu\nu_{LT} - \nu)E_L E_T - \nu_{LT}^2 E_T^2}{E_L(1-\nu^2) - 2E_T\nu_{LT}^2(1+\nu)} \\ \beta &= \frac{(1-\nu^2)E_L^2 + \nu_{LT}^2 E_T^2 + (\nu - 2\nu_{LT}(1+\nu))E_L E_T}{E_L(1-\nu^2) - 2E_T\nu_{LT}^2(1+\nu)} \\ &\quad - 4G_{LT} + \frac{E_T}{1+\nu} \end{aligned} \tag{4}$$

where the subscript L refers to the fibres' direction, and T to the transverse plane normal to it. Notice that the anisotropy to isotropy transiton is obtained by setting $E_L = E_T \equiv E$, $\nu_{LT} = \nu$ and $G_{LT} = E/2(1+\nu)$. The above five elastic constants then collapse to the well-known two Lamé coefficients of isotropy.

To go further, the stress tensor can be decomposed as, see (Spencer, 1984)

$$\boldsymbol{\sigma} \,=\, \boldsymbol{s} \,+\, p\mathbf{1} \,+\, t\boldsymbol{M} \tag{5}$$

where the scalar stress quantities p and t are determined by imposing the conditions $\mathrm{tr}[\boldsymbol{s}] = 0$ and $[\boldsymbol{s} : \boldsymbol{M}] = 0$. It is then easily deduced that

$$p \,=\, \frac{1}{2}\Big[\boldsymbol{\sigma} : (\mathbf{1} - \boldsymbol{M})\Big] \quad \text{and} \quad t = \frac{1}{2}\Big[\boldsymbol{\sigma} : (3\boldsymbol{M} - \mathbf{1})\Big] \tag{6}$$

and it follows by eliminating p and t from Eq. (5) that $\boldsymbol{s}$ can be written as $\boldsymbol{s} = \mathbb{P} : \boldsymbol{\sigma}$, where $\mathbb{P}$ is the pseudo-deviatoric fourth-order projection operator in the three-dimensional space given by

$$\mathbb{P} \,=\, \boldsymbol{I} - \frac{1}{2}\mathbf{1} \otimes \mathbf{1} - \frac{3}{2}\boldsymbol{M} \otimes \boldsymbol{M} + \frac{1}{2}\Big\{\boldsymbol{M} \otimes \mathbf{1} + \mathbf{1} \otimes \boldsymbol{M}\Big\} \tag{7}$$

Likewise for the strain tensor, an analogous decomposition has been applied in (Nedjar, 2011). We write

$$\boldsymbol{\varepsilon} \,=\, \boldsymbol{e} \,+\, \vartheta\mathbf{1} \,+\, \zeta\boldsymbol{M} \tag{8}$$

where $\boldsymbol{e}$ is the pseudo-deviatoric strain tensor given by $\boldsymbol{e} = \mathbb{P} : \boldsymbol{\varepsilon}$, and the scalar strain quantities ϑ and ζ are similarly determined by imposing the conditions $\mathrm{tr}[\boldsymbol{e}] = 0$ and $[\boldsymbol{e} : \boldsymbol{M}] = 0$.

Now replacing the decompositions (5) and (8) into the constitutive equation (3), one can easily extract the remarkable pseudo-deviatoric stress-strain constitutive relation

$$\boldsymbol{s} \,=\, 2\mu_T\, \boldsymbol{e} \,+\, 2(\mu_L - \mu_T)\Big\{\boldsymbol{M}\boldsymbol{e} + \boldsymbol{e}\boldsymbol{M}\Big\} \tag{9}$$

Observe that, among the set of five elastic constants, this latter depends solely on the shear moduli. It is this important fact that is exploited later

on for the viscoelastic modeling in pure shear. For later use, Eq. (9) is equivalently rewritten as

$$\boldsymbol{s} = \underbrace{\Big[2\mu_T \boldsymbol{I} + 2(\mu_L - \mu_T)\boldsymbol{I}_F\Big]}_{=\mathbf{C}_s} : \boldsymbol{e} \tag{10}$$

where we have introduced the elastic shear tensor $\mathbf{C}_s$. The fourth-order tensor $\boldsymbol{I}_F$ is such that $\boldsymbol{I}_F : \boldsymbol{e} = \boldsymbol{M}\boldsymbol{e} + \boldsymbol{e}\boldsymbol{M}$ with components

$$\left(\boldsymbol{I}_F\right)_{ijkl} = \frac{1}{2}\left(V_i V_k \delta_{jl} + V_i V_l \delta_{jk} + V_j V_l \delta_{ik} + V_k V_j \delta_{il}\right) \tag{11}$$

The complementary relation can be given in the form of a $(p,t) - (\vartheta,\zeta)$ relation as in (Nedjar, 2011). However, the equivalent one with direct use of the total strain tensor is more convenient for the following developments

$$\begin{aligned} p &= \chi_1 \,\mathrm{tr}[\boldsymbol{\varepsilon}] + \chi_2 \,[\boldsymbol{\varepsilon} : \boldsymbol{M}] \\ t &= \chi_2 \,\mathrm{tr}[\boldsymbol{\varepsilon}] + \chi_3 \,[\boldsymbol{\varepsilon} : \boldsymbol{M}] \end{aligned} \tag{12}$$

where $\chi_1 = \lambda + \mu_T$, $\chi_2 = \alpha - \mu_T$, and $\chi_3 = \beta + 4\mu_L - \mu_T$.

3. Modeling of debonding embedded into a viscoelastic matrix

In order to provide tools for structural simulations, debonding is here described by means of an internal variable modeling framework based on the plasticity theory. The plastic part of the strain tensor $\boldsymbol{\varepsilon}^{\mathrm{p}}$ is then introduced and, among others, it remains now to characterize a form for the yield criterion together with companion flow rules to describe the way debonding takes place. More specifically, in this work, focus is made on the particular cases of dominant mode-I conditions where debonding is mostly governed by tensile

stresses that are normal to the fibres. Mode-II and mixed-I/II debonding modes as developed in (Nedjar, 2014) are out of the scope of this paper.

The fibre sub-space being spanned by the tensor of the micro-structure $\boldsymbol{M}$, the projection $[\boldsymbol{\sigma} : \boldsymbol{M}] \equiv \vec{V}.\boldsymbol{\sigma}\vec{V}$ is no more than the stress along the fibres. Hence, we can deduce that the projection on the complementary sub-space gives a measure of the stress state *transverse* to the fibres, *i.e.* $[\boldsymbol{\sigma} : (\mathbf{1} - \boldsymbol{M})]$. Remarkably, this latter is precisely the definition of the stress quantity p in the decomposition (5), up to the factor $1/2$ for $n_{\text{dim}} = 3$, see Eq. $(6)_1$. Therefore, p constitutes an excellent candidate to govern this debonding mode.

Remark 1. In the two-dimensional case with a fibre direction given by $\vec{V} = \cos\theta\,\vec{e}_1 + \sin\theta\,\vec{e}_2$, where θ is the angle between the fibres and the coordinate axis $\vec{e}_1$, the stress quantity p for a general state of stress is given by, see Eq. $(A.3)_1$ in Appendix A

$$p \;=\; \sigma_{11}\,\sin^2\theta \;+\; \sigma_{22}\,\cos^2\theta \;-\; \sigma_{12}\,\sin 2\theta \tag{13}$$

which is exactly the normal stress on a face with a unit vector normal to it that makes an angle of $\theta + \pi/2$, c.f. the Mohr circle. □

3.1. Characterization of debonding

To make matters as concrete as possible in the following developments, we consider a simple, but not less efficient, model example with a p-dependent yield criterion given by

$$\mathcal{F}(p,\xi) \;=\; p \;-\; p_y \exp[-K\xi] \tag{14}$$

where the additional strain-like internal variable ξ characterizes isotropic hardening. Both p_y and K are material constants, $p_y > 0$ is the transverse flow stress, and the non-dimensional parameter K controls softening (for $K > 0$) or hardening (for $K < 0$).

Now by choosing an associated plastic flow, debonding is then given by the following evolution equations

$$\begin{cases} \dot{\boldsymbol{\varepsilon}}^{\mathrm{p}} = \gamma \dfrac{\partial \mathcal{F}}{\partial \boldsymbol{\sigma}} \equiv \dfrac{\gamma}{2}(\mathbf{1} - \boldsymbol{M}) \\ \dot{\xi} = \gamma \\ \gamma \geq 0, \quad \mathcal{F}(p, \xi) \leq 0, \quad \gamma \mathcal{F}(p, \xi) = 0 \end{cases} \tag{15}$$

where γ is the consistency parameter that satisfies the Kuhn-Tucker loading/unloading conditions $(15)_3$. In the evaluation $(15)_1$, use has been made of the relation $(6)_1$. This would be $\dot{\boldsymbol{\varepsilon}}^{\mathrm{p}} = \gamma(\mathbf{1} - \boldsymbol{M})$ for the plane-stress case, see Eq. $(A.3)_1$. Anyhow, and irrespective to the space dimension of the problem, one has the following remarkable properties

$$\mathrm{tr}[\dot{\boldsymbol{\varepsilon}}^{\mathrm{p}}] = \gamma \qquad [\dot{\boldsymbol{\varepsilon}}^{\mathrm{p}} : \boldsymbol{M}] = 0 \qquad \dot{\boldsymbol{e}}^{\mathrm{p}} = \mathbf{0} \tag{16}$$

where $\boldsymbol{e}^{\mathrm{p}}$ is the pseudo-deviatoric part of $\boldsymbol{\varepsilon}^{\mathrm{p}}$. Hence, plastic straining solely affects the trace term while $\boldsymbol{e}^{\mathrm{p}}$ remains inactive.

3.2. Characterization of viscoelasticity in pure shear

On another hand, considering that the matrix can otherwise experience creep only in shear, this condition has recently been captured within the present integrity-basis formulation in (Nedjar, 2011). We assume viscoelasticity only through the pseudo-deviatoric part of the behavior, Eq. (9) or

(10), by introducing a viscous strain tensor $\boldsymbol{e}^{\mathrm{v}}$. This latter can in turn be the sum of as many as necessary internal contributions $\boldsymbol{e}_i^{\mathrm{v}}$, *i.e.*

$$\boldsymbol{e}^{\mathrm{v}} = \sum_{i=1}^{l} \boldsymbol{e}_i^{\mathrm{v}} \tag{17}$$

where the $i = 1, \ldots, l$ hidden tensors $\boldsymbol{e}_i^{\mathrm{v}}$ characterize viscoelastic processes. An equivalent description via external variables by means of relaxation/creep functions is possible as well, see for example (Ascione et al., 2012; Ohno et al., 2002) among others.

Among the many possibilities, we choose for the evolution of the above processes the well known generalized Kelvin-Voigt rheological model. For an illustration, this device is shown in Figure 1 where the modulus μ can either be the shear modulus along the fibres μ_L or the one normal to them μ_T. Each viscous process i is characterized by the dimensionless stiffness factor ω_i and the relaxation time τ_i.

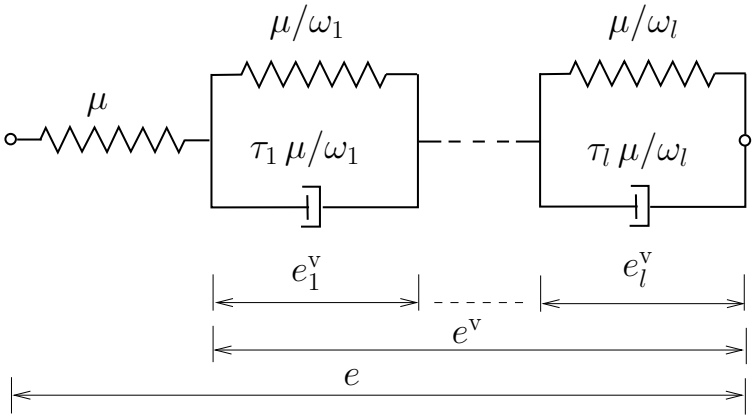

Figure 1: Generalized Kelvin-Voigt rheological model used for the viscoelastic behavior in pure shear. Here the modulus μ is either μ_L or μ_T.

The l local evolution equations are then given by, see (Nedjar, 2011) for full details,

$$\dot{\boldsymbol{e}}_i^{\mathrm{v}} \,+\, \frac{1}{\tau_i}\,\boldsymbol{e}_i^{\mathrm{v}} \,+\, \frac{\omega_i}{\tau_i}\sum_{j=1}^{l}\boldsymbol{e}_j^{\mathrm{v}} \,=\, \frac{\omega_i}{\tau_i}\,\boldsymbol{e}, \qquad i=1,\ldots,l \tag{18}$$

where no sum on repeated indices is assumed in Eq. (18). Notice that, by construction, the internal variables $\boldsymbol{e}_i^{\mathrm{v}}$ satisfy the conditions $\mathrm{tr}[\boldsymbol{e}_i^{\mathrm{v}}]=0$ and $[\boldsymbol{e}_i^{\mathrm{v}}:\boldsymbol{M}]=0$. One has then for the total viscoelastic strain tensor

$$\mathrm{tr}[\boldsymbol{e}^{\mathrm{v}}]=0 \qquad [\boldsymbol{e}^{\mathrm{v}}:\boldsymbol{M}]=0 \tag{19}$$

3.3. Recapitulation and basic constitutive equations

With the properties (16) and (19), the elastic parts of the stress-strain constitutive relation, Eqs. (10) and (12), become for the present viscoelastic model coupled with debonding

$$\begin{aligned}
\boldsymbol{s} &= \mathbf{C}_s:(\boldsymbol{e}-\boldsymbol{e}^{\mathrm{v}}) \\
p &= \chi_1\,(\mathrm{tr}[\boldsymbol{\varepsilon}]-\mathrm{tr}[\boldsymbol{\varepsilon}^{\mathrm{p}}]) \,+\, \chi_2\,[\boldsymbol{\varepsilon}:\boldsymbol{M}] \\
t &= \chi_2\,(\mathrm{tr}[\boldsymbol{\varepsilon}]-\mathrm{tr}[\boldsymbol{\varepsilon}^{\mathrm{p}}]) \,+\, \chi_3\,[\boldsymbol{\varepsilon}:\boldsymbol{M}]
\end{aligned} \tag{20}$$

Hence, the behavior in pure shear remains viscoelastic while the plasticity only affects the *scalar* trace terms in the definition of the stress components p and t. These remarkable facts drastically simplify the plastic and viscoelastic updates within the algorithmic scheme as shown below.

In summary: the fibre/matrix debonding with matrix creep is described by the constitutive equations (5) and (20), the l local evolution equations (18) for the matrix creep in pure shear, and the local problem (14)-(15) for the mode-I debonding.

4. Time integration and numerical implementation

The key idea in the design of the integration algorithm is to exploit the fact that the l viscoelastic evolution equations (18) are independent of the mode-I debonding, and vice versa. It is then carried out by the combination of algorithms, each one adapted to the corresponding sub-problem. The order in which these algorithms are sequenced is not important.

In a finite element context, the approximation of the above evolution equations is accomplished at the integration point level. Within a typical time interval $[t_n, t_{n+1}]$ with $\Delta t = t_{n+1} - t_n$, the sets of internal variables $\{\boldsymbol{\varepsilon}^{\mathrm{p}}_n, \xi_n\}$ and $\{\boldsymbol{e}^{\mathrm{v}}_{i\,n}, i = 1, \ldots, l\}$ are known at time t_n. The objective is to advance the solution to time t_{n+1} and update the variables to $\{\boldsymbol{\varepsilon}^{\mathrm{p}}_{n+1}, \xi_{n+1}\}$ and $\{\boldsymbol{e}^{\mathrm{v}}_{i\,n+1}, i = 1, \ldots, l\}$ through a strain driven procedure since the incremented total strain tensor $\boldsymbol{\varepsilon}_{n+1}$ is known during the iterative process.

4.1. Numerical integration of debonding

For the plasticiy-based debonding model, we use the well-known elastic predictor/plastic corrector concept. A backward-Euler scheme is applied to the constrained evolution equations (15) to give the incremental forms

$$\left\{\begin{array}{l} \mathrm{tr}[\boldsymbol{\varepsilon}^{\mathrm{p}}_{n+1}] \;=\; \mathrm{tr}[\boldsymbol{\varepsilon}^{\mathrm{p}}_{n}] + \Delta\gamma \\ \xi_{n+1} \;=\; \xi_n + \Delta\gamma \\ \Delta\gamma \geq 0, \quad \mathcal{F}_{n+1} \leq 0, \quad \Delta\gamma\mathcal{F}_{n+1} = 0 \end{array}\right. \tag{21}$$

where use has been made of the property $(16)_1$. We have used the notations $\Delta\gamma = \gamma\Delta t$ and $\mathcal{F}_{n+1} = \mathcal{F}(p_{n+1}, \xi_{n+1})$.

Firstly, the yield criterion (14) is evaluated at the trial state as $\mathcal{F}_{n+1}^{\text{trial}} \equiv \mathcal{F}(p_{n+1}^{\text{trial}}, \xi_n)$ where the trial p-stress component is given by

$$p_{n+1}^{\text{trial}} = \chi_1 \left(\text{tr}[\boldsymbol{\varepsilon}_{n+1}] - \text{tr}[\boldsymbol{\varepsilon}_n^{\text{p}}]\right) + \chi_2 \left[\boldsymbol{\varepsilon}_{n+1} : \boldsymbol{M}\right] \tag{22}$$

Hence, if $\mathcal{F}_{n+1}^{\text{trial}} \leq 0$, the trial state is admissible and we set $\boldsymbol{\varepsilon}_{n+1}^{\text{p}} = \boldsymbol{\varepsilon}_n^{\text{p}}$ and $\xi_{n+1} = \xi_n$. Otherwise, the trial state is not admissible and a correction has to be performed. This is accomplished by noticing that, at the final state, the converged transvese stress measure p_{n+1} is simply given by

$$p_{n+1} = p_{n+1}^{\text{trial}} - \chi_1 \Delta\gamma \tag{23}$$

Then, enforcing the consistency condition $\mathcal{F}_{n+1} = 0$ at time t_{n+1}, in combination with (23) and $(21)_2$, lead to the following nonlinear equation to be solved for $\Delta\gamma > 0$ by means of a Newton scheme

$$p_{n+1}^{\text{trial}} - \chi_1 \Delta\gamma - p_y \exp[-K\xi_n] \exp[-K\Delta\gamma] = 0 \tag{24}$$

which, for the case of perfect plasticity with $K = 0$, gives the closed-form solution $\Delta\gamma = \mathcal{F}_{n+1}^{\text{trial}}/\chi_1$. The plastic updates then follow by replacing the above solution $\Delta\gamma$ in the discrete equations $(21)_{1-2}$.

However, it is nowadays well known that strain-softening can render the global initial boundary value problem ill-posed, *i.e.* with $K > 0$ for our yield criterion, Eq. (14). One way to circumvent this difficulty is the use of a time-dependent regularization. A viscoplastic model can readily be obtained through a Perzyna-type regularization (Perzyna, 1971) or a Duvaut-Lions-type regularization (Duvaut and Lions, 1972). For extensive discussions on this topic, the reader is referred to (Simo and Hughes, 1998), among others. In this work, a Duvaut-Lions regularization is constructed as follows.

After having solved for the inviscid solution, *i.e.* the above updates $\mathrm{tr}[\boldsymbol{\varepsilon}^{\mathrm{p}}_{n+1}]$ and ξ_{n+1}, we define viscous counterpart quantities $\mathrm{tr}[\boldsymbol{\varepsilon}^{\mathrm{vp}}]$ and ξ^{v} as

$$\left\{\begin{array}{l} \mathrm{tr}[\dot{\boldsymbol{\varepsilon}}^{\mathrm{vp}}] \,=\, \dfrac{1}{\eta}\Big(\mathrm{tr}[\boldsymbol{\varepsilon}^{\mathrm{p}}_{n+1}] - \mathrm{tr}[\boldsymbol{\varepsilon}^{\mathrm{vp}}]\Big) \\ \dot{\xi}^{\mathrm{v}} \,=\, \dfrac{1}{\eta}\Big(\xi_{n+1} - \xi^{\mathrm{v}}\Big) \end{array}\right. \tag{25}$$

where η is a fluidity parameter with the time as dimension. These equations may in turn be discretized, here by using again the backward-Euler scheme to get

$$\left\{\begin{array}{l} \Big(1+\dfrac{\Delta t}{\eta}\Big)\,\mathrm{tr}[\boldsymbol{\varepsilon}^{\mathrm{vp}}_{n+1}] \,=\, \mathrm{tr}[\boldsymbol{\varepsilon}^{\mathrm{vp}}_{n}] \,+\, \dfrac{\Delta t}{\eta}\,\mathrm{tr}[\boldsymbol{\varepsilon}^{\mathrm{p}}_{n+1}] \\ \Big(1+\dfrac{\Delta t}{\eta}\Big)\,\xi^{\mathrm{v}}_{n+1} \,=\, \xi^{\mathrm{v}}_{n} \,+\, \dfrac{\Delta t}{\eta}\,\xi_{n+1} \end{array}\right. \tag{26}$$

Now by replacing the discrete forms $(21)_{1-2}$ into (26), and after noticing that this time we have $\mathrm{tr}[\boldsymbol{\varepsilon}^{\mathrm{vp}}_{n}] = \mathrm{tr}[\boldsymbol{\varepsilon}^{\mathrm{p}}_{n}]$ and $\xi^{\mathrm{v}}_{n} = \xi_n$, we get the update formulae

$$\left\{\begin{array}{l} \mathrm{tr}[\boldsymbol{\varepsilon}^{\mathrm{vp}}_{n+1}] \,=\, \mathrm{tr}[\boldsymbol{\varepsilon}^{\mathrm{vp}}_{n}] + \varpi\,\Delta\gamma \\ \xi^{\mathrm{v}}_{n+1} \,=\, \xi^{\mathrm{v}}_{n} + \varpi\,\Delta\gamma \end{array}\right. \tag{27}$$

where we have introduced the notation

$$\varpi \,=\, \frac{\Delta t}{\eta + \Delta t} \tag{28}$$

In this form, the algorithm is adapted to both viscoplasticity and rate-independent plasticity. This latter is recovered simply by setting $\eta = 0 \Rightarrow \varpi = 1$ in the update formulae. For the sake of clarity, Table 1 summarizes the conceptual steps involved during this local resolution procedure.

Table 1: Local algorithm for mode-I debonding.

1. Trial state:

$$\boldsymbol{s}_{n+1} = \mathbf{C}_s : (\boldsymbol{e}_{n+1} - \boldsymbol{e}^{\mathrm{v}}_{n+1}) \equiv \boldsymbol{s}_{n+1} \text{ from viscoelasticity}$$

$$p^{\mathrm{trial}}_{n+1} = \chi_1 \left(\mathrm{tr}[\boldsymbol{\varepsilon}_{n+1}] - \mathrm{tr}[\boldsymbol{\varepsilon}^{\mathrm{p}}_n]\right) + \chi_2 \left[\boldsymbol{\varepsilon}_{n+1} : \boldsymbol{M}\right]$$

$$t^{\mathrm{trial}}_{n+1} = \chi_2 \left(\mathrm{tr}[\boldsymbol{\varepsilon}_{n+1}] - \mathrm{tr}[\boldsymbol{\varepsilon}^{\mathrm{p}}_n]\right) + \chi_3 \left[\boldsymbol{\varepsilon}_{n+1} : \boldsymbol{M}\right]$$

$$\mathcal{F}^{\mathrm{trial}}_{n+1} = p^{\mathrm{trial}}_{n+1} - p_y \exp[-K\xi_n]$$

2. IF $\mathcal{F}^{\mathrm{trial}}_{n+1} \leq 0$ THEN

set: $\boldsymbol{\varepsilon}^{\mathrm{p}}_{n+1} = \boldsymbol{\varepsilon}^{\mathrm{p}}_n$, $\xi_{n+1} = \xi_n$, $p_{n+1} = p^{\mathrm{trial}}_{n+1}$, $t_{n+1} = t^{\mathrm{trial}}_{n+1}$

ELSE IF $\mathcal{F}^{\mathrm{trial}}_{n+1} > 0$ THEN

solve $\mathcal{F}_{n+1} = 0$ for $\Delta\gamma$, Equation (24)

update the internal variables:

$$\begin{cases} \mathrm{tr}[\boldsymbol{\varepsilon}^{\mathrm{p}}_{n+1}] \;=\; \mathrm{tr}[\boldsymbol{\varepsilon}^{\mathrm{p}}_n] + \varpi\, \Delta\gamma \\ \xi_{n+1} \;=\; \xi_n + \varpi\, \Delta\gamma \end{cases}$$

with $\varpi = \Delta t/(\eta + \Delta t)$

update the stress components:

$$p_{n+1} = p^{\mathrm{trial}}_{n+1} - \varpi\, \Delta\gamma\, \chi_1$$

$$t_{n+1} = t^{\mathrm{trial}}_{n+1} - \varpi\, \Delta\gamma\, \chi_2$$

END IF

3. Reconstitute the total stress tensor:

$$\boldsymbol{\sigma}_{n+1} = \boldsymbol{s}_{n+1} + p_{n+1}\mathbf{1} + t_{n+1}\boldsymbol{M}$$

4.2. Outlines of the viscoelastic integration

The incremented total strain tensor $\boldsymbol{\varepsilon}_{n+1}$ being known, so is the pseudo-deviatoric strain tensor $\boldsymbol{e}_{n+1}$. The internal variables $\boldsymbol{e}^{\mathrm{v}}_{i\,n}$, $i = 1, \ldots, l$ at time t_n can be updated to $\boldsymbol{e}^{\mathrm{v}}_{i\,n+1}$ through either a fully implicit scheme or a semi-implicit one combined with the exponential map, see (Nedjar, 2011) for details about these two schemes. For instance, when the latter is applied to the l evolution equations (18), this leads to the following decoupled update

$$\begin{aligned} \boldsymbol{e}^{\mathrm{v}}_{i\,n+1} &= \frac{\omega_i}{1+\omega_i}\Big\{\boldsymbol{e}_{n+1} - \sum_{j=1, j\neq i}^{l} \boldsymbol{e}^{\mathrm{v}}_{j\,n}\Big\}\big(1-\exp(-\alpha_i \Delta t)\big) \\ &+ \boldsymbol{e}^{\mathrm{v}}_{i\,n}\,\exp(-\alpha_i \Delta t), \qquad i = 1, \ldots, l \end{aligned} \tag{29}$$

where we have introduced the notation $\alpha_i = (1+\omega_i)/\tau_i$.

For later use, the algorithmic rate of change of the viscoelastic internal variables in terms of the rate of change of the pseudo-deviatoric tensor is computed from Eq. (29) as

$$\dot{\boldsymbol{e}}^{\mathrm{v}}_{i} = \frac{\omega_i}{1+\omega_i}\big(1-\exp(-\alpha_i \Delta t)\big)\,\dot{\boldsymbol{e}}, \qquad i = 1, \ldots, l \tag{30}$$

so that, by Eq. (17), the algorithmic rate of change of the viscoelastic strain tensor is given by

$$\dot{\boldsymbol{e}}^{\mathrm{v}} = \underbrace{\left(\sum_{i=1}^{l} \frac{\omega_i}{1+\omega_i}\big(1-\exp(-\alpha_i \Delta t)\big)\right)}_{=\,\hat{\delta}}\,\dot{\boldsymbol{e}} \tag{31}$$

where the notation $\hat{\delta}$ has been introduced. See (Nedjar, 2011) for the corresponding expressions when the fully implicit scheme is used instead.

4.3. Algorithmic tangent moduli

The nonlinear initial boundary-value problem at hand is here solved by means of an iterative procedure of the Newton's type. Accordingly, this requires the linearization of the global equilibrium about a known state at time t_n. This procedure is nowadays standard and we give in this section the contribution to the algorithmic tangent stiffness where it is of interest to determine the relation between the rate of stress and the rate of *total* strain via the algorithmic change of the internal variables $\boldsymbol{\varepsilon}^{\mathrm{p}}, \xi$ and $\{\boldsymbol{e}_i^{\mathrm{v}}, i = 1, \ldots, l\}$. That is, to find the tangent modulus $\mathbf{C}_{n+1}^{\mathrm{algo}}$ such that

$$\dot{\boldsymbol{\sigma}}_{n+1} \,=\, \mathbf{C}_{n+1}^{\mathrm{algo}} : \dot{\boldsymbol{\varepsilon}}_{n+1} \tag{32}$$

When debonding takes place, the updated stress is given by, see Table 1,

$$\begin{aligned} \boldsymbol{\sigma}_{n+1} \;&=\; \mathbf{C}_s : \boldsymbol{e}_{n+1} \,+\, p_{n+1}^{\mathrm{trial}} \mathbf{1} \,+\, t_{n+1}^{\mathrm{trial}} \boldsymbol{M} \\ &-\; \mathbf{C}_s : \boldsymbol{e}_{n+1}^{\mathrm{v}} \,-\, \varpi\, \Delta\gamma \Big\{ \chi_1 \mathbf{1} + \chi_2 \boldsymbol{M} \Big\} \end{aligned} \tag{33}$$

The rate form of the first three terms in the right hand side of Eq. (33) is no more than $\mathbf{H}_{\mathrm{ani}} : \dot{\boldsymbol{\varepsilon}}_{n+1}$, where $\mathbf{H}_{\mathrm{ani}}$ is the constant transversely isotropic elastic Hooke's tensor given by, see Eq. (3),

$$\mathbf{H}_{\mathrm{ani}} \,=\, \lambda \mathbf{1} \otimes \mathbf{1} \,+\, \beta \boldsymbol{M} \otimes \boldsymbol{M} \,+\, \alpha \Big\{ \mathbf{1} \otimes \boldsymbol{M} + \boldsymbol{M} \otimes \mathbf{1} \Big\} \,+\, \mathbf{C}_s \tag{34}$$

The rate form of the fourth term in the right hand side of Eq. (33) is computed with the help of the algorithmic relation (31) together with the pseudo-deviatoric projection $\dot{\boldsymbol{e}}_{n+1} = \mathbb{P} : \dot{\boldsymbol{\varepsilon}}_{n+1}$. Finally, for the last term in Eq. (33), the chain rule is employed where the derivative $\partial \Delta\gamma / \partial \boldsymbol{\varepsilon}_{n+1}$ is obtained

by linearizing the consistency condition enforcement, Eq. (24), which gives

$$\underbrace{\Big(\chi_1 - Kp_y \exp[-K\xi_{n+1}]\Big)}_{=\varkappa_{n+1}} \frac{\partial \Delta\gamma}{\partial \boldsymbol{\varepsilon}_{n+1}} \;=\; \chi_1 \mathbf{1} + \chi_2 \boldsymbol{M} \tag{35}$$

where the notation $\varkappa$ has been introduced for convenience.

With these partial relations, the symmetric algorithmic tangent modulus is then reconstitued as

$$\begin{aligned} \mathbf{C}^{\text{algo}}_{n+1} \;=\; & \mathbf{H}_{\text{ani}} \;-\; \underbrace{\hat{\delta}\Big\{2\mu_T \mathbb{P} + 2(\mu_L - \mu_T)\boldsymbol{I}_F - 4(\mu_L - \mu_T)\boldsymbol{M}\otimes\boldsymbol{M}\Big\}}_{\textsf{viscoelasticity}} \\ & -\; \underbrace{\frac{\varpi}{\varkappa_{n+1}}\Big\{\chi_1\mathbf{1} + \chi_2\boldsymbol{M}\Big\}\otimes\Big\{\chi_1\mathbf{1} + \chi_2\boldsymbol{M}\Big\}}_{\textsf{debonding}} \end{aligned} \tag{36}$$

5. Representative numerical examples

The theory developed in this work has been implemented in a finite element software where new routines have been coded. We give in this section numerical simulations that demonstrate the effectiveness of the proposed framework. The examples are related to the frequently encountered situations of dominant mode-I debonding conditions that fall within the scope of this work. Among others, we show the strong influence of the fibres' direction on the responses predicted by the model.

5.1. Three-points bending tests on single-edge notched specimens

We consider in this section plate samples of dimensions $(50\times 11)\,mm^2$ and $1\,mm$ thickness with a notch of $2.5\,mm$ length and $0.4\,mm$ width centered at one edge, while the center of the opposite edge constitutes the point-load for the bending tests. The direction of the fibres is characterized by

the angle θ with respect to the global $\vec{e}_1$-axis as illustrated in Figure 2. Plane-stress assumption is considered in this analysis, see Appendix A for related complementary details. This example has been motivated by the experimental investigations in (Lee et al., 2010) on similar samples where the authors have studied the fracture behavior of unidirectional graphite composite laminates by means of a 2D digital image correlation method.

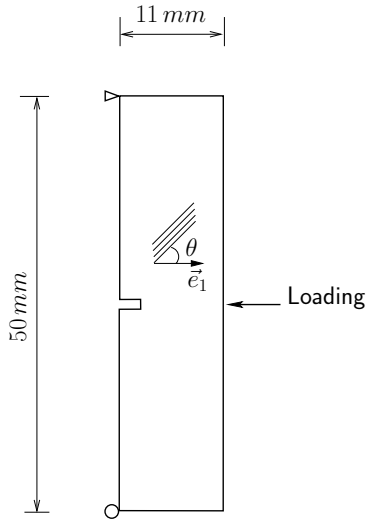

Figure 2: Sample specimen with a notch. Geometry and boundary conditions.

For the unidirectional composite material, the elastic characteristics we use are those of the graphite/epoxy given in (Lee et al., 2010). They are listed in Table 2 where formulae (4) have been used to obtain the corresponding Lamé-like coefficients. For debonding, we choose the following transverse flow stress and hardening/softening control parameter

$$p_y = 5\,MPa \qquad K = 100 \tag{37}$$

Table 2: Elastic characteristics of the UD composite.

Engineering parameters	Lamé-like coefficients
$E_L = 171.6\,GPa$	$\lambda = 0.214\,GPa$
$E_T = 8.25\,GPa$	$\mu_T = 4.044\,GPa$
$G_{LT} = 6.21\,GPa$	$\mu_L = 6.21\,GPa$
$\nu_{LT} = 0.344$	$\beta = 151.219\,GPa$
$\nu = 0.02$	$\alpha = 2.715\,GPa$

where a plastic-softening is induced with $K > 0$ so as to trigger a pic-load for the specimen's response. In all the computations that will follow, we use a fluidity parameter $\eta = 10^{-3}s$ for the viscoplastic regularization.

Now for the viscoelastic behavior in pure shear, we choose to activate two processes, *i.e.* $l = 2$, and fix their couples of parameters as

$$(\omega_1 = 2.5, \tau_1 = 10^2[T]) \qquad (\omega_2 = 4, \tau_2 = 10^4[T]) \tag{38}$$

where, and as this is only for illustrative purposes, $[T]$ denotes the unit of time (seconds, hours, ...). Let us recall that, after complete relaxation, the instantaneous effective shear moduli μ_L and μ_T become, respectively,

$$\frac{\mu_L}{1+\omega_1+\omega_2} \qquad \text{and} \qquad \frac{\mu_T}{1+\omega_1+\omega_2} \tag{39}$$

when $t \to \infty$.

Furthermore, to show the numerical behavior of the finite element implementation, three mesh refinements are used with growing density around the tip of the notch; mesh-1 with 2550 elements, mesh-2 with 4282 elements,

and mesh-3 with 7894 elements. All the computations use the standard displacement-based triangular element with a quadratic interpolation Tri6.

In a first step, and for a given fibres' orientation, we need to determine the short-term strength of the specimen in three-points bending conditions. For this, the viscoelastic part of the behavior is deactivated and the response is computed under monotonic loading by prescribing an increasing displacement of the point-load. Figure 3 shows the results for the fibres' directions $\theta = 0°$, $30°$ and $45°$. Each case has in turn been computed with the three aforementioned finite element meshes. One can observe the good convergence properties, at least until the pic-loads. The two denser meshes show close responses while mesh-1 gives higher pic-loads in all cases. The strengths R_0, R_{30} and R_{45} are then the pic-load values of the curves obtained with the denser mesh, *i.e.* mesh-3. In particular for later use, we have obtained $R_{30} = 6.29\,N$ and $R_{45} = 9.94\,N$.

Now for the long-term response with active viscoelastic behavior in pure shear, Figure 4 shows the results of two creep tests for the fibre orientations $\theta = 30°$ and $\theta = 45°$ at constant loads corresponding to 70% of their respective strengths, see the marked points illustrated in Figure 3. Each test has been computed with the above two denser mesh refinements, mesh-2 and mesh-3. The curves represent the evolution of the point-load displacement with respect to time. In both cases we obtain the typical S-shaped form highlighting three stages corresponding to a primary creep, a more or less pseudo-linear secondary creep, and a fast tertiary creep before failure. For the sake of comparison, similar computations ignoring the shear viscoelasticity give the two dashed straight lines, also plotted in Figure 4, which means

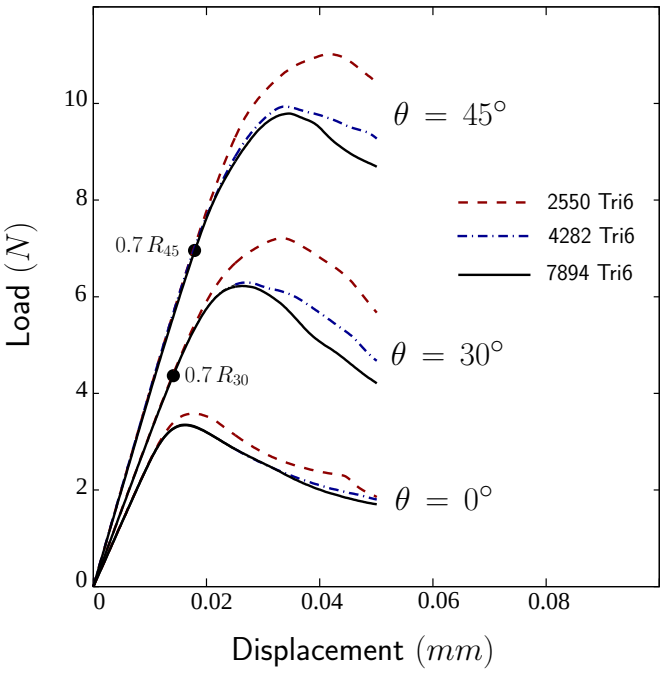

Figure 3: Short-term response in three-points bending for different orientations of the fibres. Results for three different mesh refinements.

that no debonding nor creep failure occur in this case.

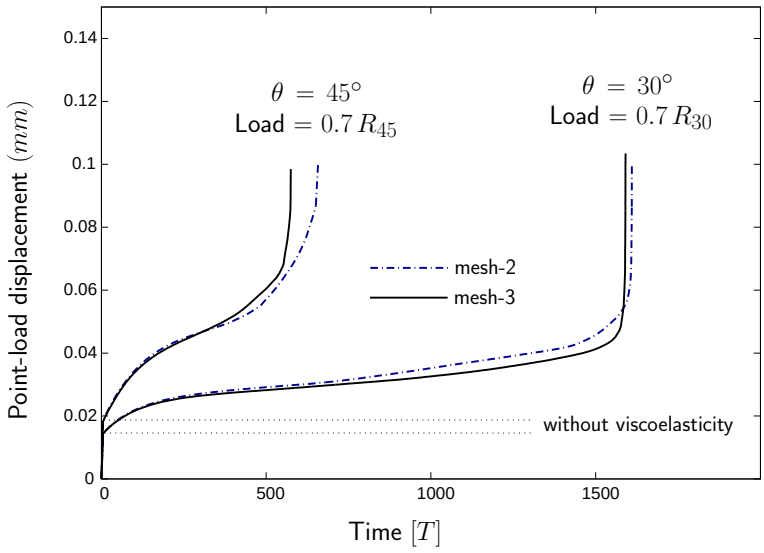

Figure 4: Creep results for $\theta = 30°$ and $\theta = 45°$ specimens under 70% of the respective strength loads.

At the local level, Figure 5 shows the computed plastic fields during the respective tertiary creep stages. For illustrative purposes, Figure 5(a) corresponds to $\theta = 30°$ computed with mesh-2, while Figure 5(b) corresponds to $\theta = 45°$ computed with mesh-3. One can observe that, in all cases, debonding emanates from the tip region of the notch and propagates along the direction of the fibres. These local results are in complete agreement with the optical observations made in (Lee et al., 2010) from similar experimental tests.

5.2. Traction of a notched strip

In this second example we consider similar computations, this time on the $(24 \times 120)\,mm^2$ rectangular strip with a centered notch of $5\,mm$ length and

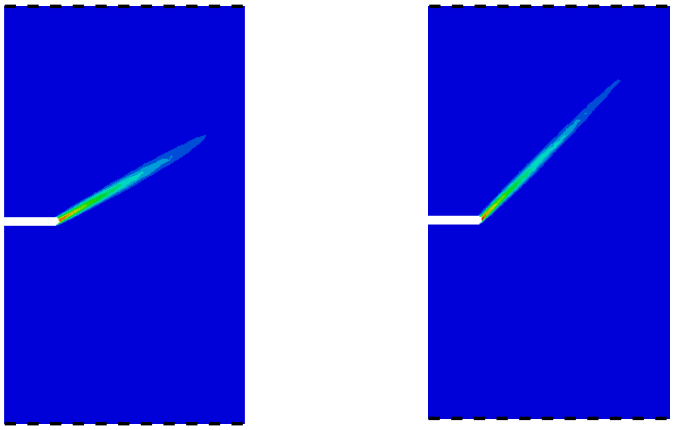

(a) $\theta = 30°$, mesh-2 (b) $\theta = 45°$, mesh-3

Figure 5: Equivalent plastic strain field at the tertiary creep: (a) for $\theta = 30°$ with mesh-2, and (b) for $\theta = 45°$ with mesh-3.

$0.04\,mm$ width as illustrated in Figure 6. The top and bottom edges are fixed along the $\vec{e}_1$-axis while loading is applied on the top edge in the direction $\vec{e}_2$. Here again the plane-stress assumption is assumed with thickness $1\,mm$. This example has been motivated by experimental and theoretical studies on unidirectional glass/epoxy composites where authors use similar specimens, see for example (Andersons et al., 2010).

For the unidirectional composite, the material characteristics we use are those given in the precedent example (Section 5.1). Figure 7 shows the results of the short-term responses for different orientations θ of the fibres with respect to the global $\vec{e}_1$-axis. As expected, we observe that the more the fibres deviate from the loading direction the more the strength of the strip decreases.

Now for long-term responses, Figure 8 illustrates the results of simulated

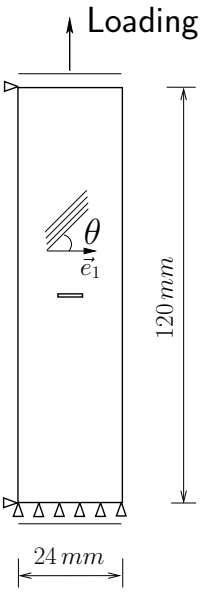

Figure 6: Rectangular specimen with a notch. Geometry and boundary conditions.

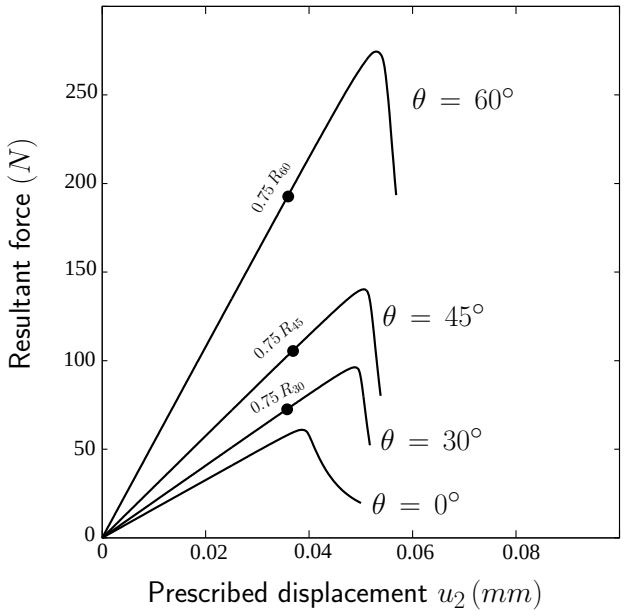

Figure 7: Short-term response of the notched strip for different orientations of the fibres.

creep tests for the fibre orientations $\theta = 30°, 45°$ and $60°$ at 75% of the respective strength loads, see the marked points in Figure 7. In this case one can observe the somehow sharp tertiaty creep before failure.

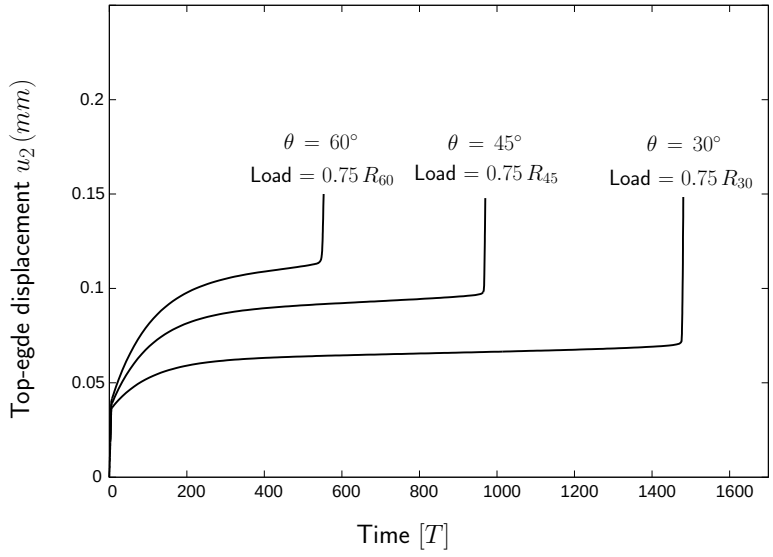

Figure 8: Creep results for $\theta = 30°, 45°$ and $60°$- strip under 75% of the respective strength loads.

Finally, at the local level, debonding path is shown in Figure 9 during the respective tertiary creep stages. Here again, one can observe that debonding emanates from the tip region of the notch and propagates along the direction of the fibres. These local results are again in agreement with experimental observations made in the literature, see for example (Andersons et al., 2010).

6. Conclusion and perspectives

The main thrust of this paper has been the formulation of a model in order to provide a tool for predicting the long-term response of unidirec-

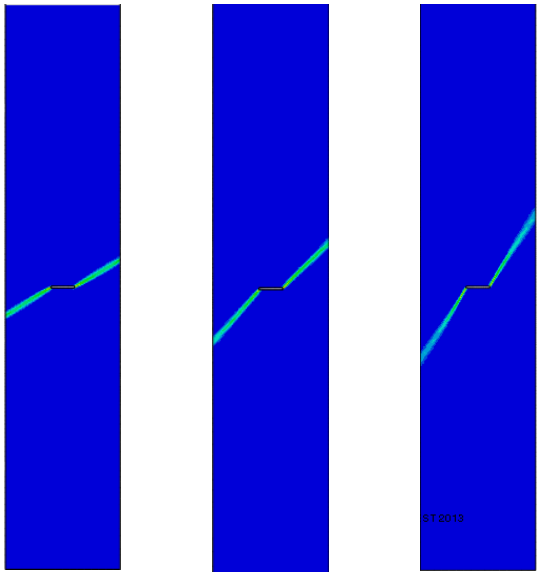

Figure 9: Debonding propagation at the tertiary creep stages for $\theta = 30°, 45°$ and $60°$.

tional fibre-reinforced composites that experience dominant mode-I debonding. The transversely isotropic behavior of the material has been captured by means of the so-called integrity-basis formulation. This latter allows for a neat decomposition of the stress and strain fields into fibre-directional, transverse, and pure shear parts. In particular, the viscous behavior is here taken into account through the shear part of the behavior, while debonding is modeled through its transverse part.

In this manner, a subtle modeling framework has been established that permits to reflect to the macroscale some important micromechanical processes such like debonding in our case. For this latter, a plasticity-based formulation has been used to build a model by means of a yield criterion governed, precisely, by the tension transverse to the fibres.

A detailed algorithmic treatment has been developed in order to numerically integrate the constitutive law and the local evolution equations at hand within the context of the finite element method. Representative numerical simulations have been performed to show the possibilities of the proposed modeling framework. In particular, the strong influence of the fibre direction on debonding propagation, on the one hand, and the ability of the model to capture long-term creep response, on the other hand, were explored and commented.

We believe that the modeling framework developed in this paper can trigger deeper research. For instance, we can extend the present model to take into account the reduction of the elastic properties with the introduction of new damage-type internal variables via the nowadays well-known formalism of continuum damage mechanics. Additional debonding modes can also be introduced, *i.e.* mode-II and mixed-I/II debonding mechanisms, and also, one can think about the combination with fibre breakage damage mode. These topics will be the subject of future investigations.

Appendix A. Two-dimensional plane-stress particularization

For the many practical applications with thin composite samples, it proves convenient to particularize the above developments for two-dimensional problems under the plane-stress assumption. Here we consider the plane spanned by the cartesian basis $\{\vec{e}_i\}_{i=1,2}$.

The problem being independent of the coordinate x_3, when introducing the constraints $\sigma_{13} = \sigma_{23} = \sigma_{33} = 0$, the constitutive relation, Eq. (3),

becomes

$$\begin{aligned}\boldsymbol{\sigma} \;=\; & \lambda\left(1-\frac{\lambda}{\lambda+2\mu_T}\right)\,\mathrm{tr}[\boldsymbol{\varepsilon}]\,\mathbf{1} \;+\; \left(\beta-\frac{\alpha^2}{\lambda+2\mu_T}\right)\,[\boldsymbol{\varepsilon}:\boldsymbol{M}]\,\boldsymbol{M} \\ & +\alpha\left(1-\frac{\lambda}{\lambda+2\mu_T}\right)\,\Big\{\mathrm{tr}[\boldsymbol{\varepsilon}]\boldsymbol{M}+[\boldsymbol{\varepsilon}:\boldsymbol{M}]\mathbf{1}\Big\} \\ & +2\,\mu_T\,\boldsymbol{\varepsilon} \;+\; 2(\mu_L-\mu_T)\Big\{\boldsymbol{M}\boldsymbol{\varepsilon}+\boldsymbol{\varepsilon}\boldsymbol{M}\Big\}\end{aligned} \tag{A.1}$$

where all the tensorial quantities are understood in two dimensions. In particular, the trace operator becomes here $\mathrm{tr}[\boldsymbol{\varepsilon}] \equiv [\boldsymbol{\varepsilon} : \mathbf{1}] = \varepsilon_{11} + \varepsilon_{22}$. The nonzero off-plane strain is given by

$$\varepsilon_{33} = -\frac{1}{\lambda+2\mu_T}\Big(\lambda\,\mathrm{tr}[\boldsymbol{\varepsilon}]+\alpha\,[\boldsymbol{\varepsilon}:\boldsymbol{M}]\Big) \tag{A.2}$$

The stress decomposition (5) gives this time

$$p \;=\; \big[\boldsymbol{\sigma}:(\mathbf{1}-\boldsymbol{M})\big] \quad \text{and} \quad t = \big[\boldsymbol{\sigma}:(2\boldsymbol{M}-\mathbf{1})\big] \tag{A.3}$$

for the scalar stress quantities, and $\boldsymbol{s}$ is now written as $\boldsymbol{s} = \bar{\mathbb{P}}:\boldsymbol{\sigma}$, where the fourth-order projection operator in the two-dimensional space is given by

$$\bar{\mathbb{P}} \;=\; \boldsymbol{I}-\mathbf{1}\otimes\mathbf{1}-2\boldsymbol{M}\otimes\boldsymbol{M}+\Big\{\boldsymbol{M}\otimes\mathbf{1}+\mathbf{1}\otimes\boldsymbol{M}\Big\} \tag{A.4}$$

and which should replace the operator $\mathbb{P}$ given by Eq. (6).

Likewise for the in-plane strain tensor, the decomposition (8) gives the pseudo-deviatoric part as $\boldsymbol{e} = \bar{\mathbb{P}}:\boldsymbol{\varepsilon}$, and the scalar strain quantities ϑ and ζ by similar formulas as in (A.3).

Replacing these decompositions into Eq. (A.1), the pseudo-deviatoric part of the stress-strain relation is exactly the one given by Eq. (9), and the

complementary part is given by Eqs. (12) as well, but this time with the following modified elastic coefficients

$$\begin{aligned} \chi_1 &= \lambda\left(1-\frac{\lambda}{\lambda+2\mu_T}\right)+2\mu_T \\ \chi_2 &= \alpha\left(1-\frac{\lambda}{\lambda+2\mu_T}\right)-2\mu_T \\ \chi_3 &= \beta-\frac{\alpha^2}{\lambda+2\mu_T}+4\mu_L \end{aligned} \tag{A.5}$$

which should be used in all the developments of Sections 3 and 4.

References

Andersons, J., Tarasovs, S., Spārniņš, E., 2010. Finite fracture mechanics analysis of crack onset at a stress concentration in a ud glass/epoxy composite in off-axis tension. Composites Science and Technology **70**, 1380–1385.

Ascione, L., Berardi, V., D'Aponte, A., 2012. Creep phenomena in FRP materials. Mechanics Research Communications **43**, 15–21.

Beyerlein, I., Landis, C., 1999. Shear-lag model for failure simulations of unidirectional fiber composites including matrix stiffness. Mechanics of Materials **31**, 331–350.

Bonet, J., Burton, A., 1998. A simple orthotropic, transversely isotropic hyperelastic constitutive equation for large strain computations. Computer Methods in Applied Mechanics and Engineering **162**, 151–164.

Duvaut, G., Lions, J., 1972. Les inéquations en Mécanique et en Physique. Dunod, Paris.

Holzapfel, G., 2000. Nonlinear solid mechanics. A continuum approach for engineering. John Wiley and Sons, Ltd, Chichester, West Sussex, UK.

Kaliske, M., 2000. A formulation of elasticity and viscoelasticity for fibre reinforced material at small and finite strains. Computer Methods in Applied Mechanics and Engineering **185**, 225–243.

Klinkel, S., Sansour, C., Wagner, W., 2005. An anisotropic fibre-matrix material model at finite elastic-plastic strains. Computational Mechanics **35**, 409–417.

Kurnatowski, B., Matzenmiller, A., 2012. Coupled twoscale analysis of fiber reinforced composites structures with microscopic damage evolution. International Journal of Solids and Structures **49**, 2404–2417.

Lee, D., Tippur, H., Bogert, P., 2010. Quasi-static and dynamic fracture of graphite/epoxy composites: An optical study of loading-rate effects. Composites: Part B **41**, 462–474.

Nedjar, B., 2007. An anisotropic viscoelastic fibre-matrix model at finite strains: Continuum formulation and computational aspects. Computer Methods in Applied Mechanics and Engineering **196**(9-12), 1745–1756.

Nedjar, B., 2011. A time dependent model for unidirectional fibre-reinforced composites with viscoelastic matrices. International Journal of Solids and Structures **48**, 2333–2339.

Nedjar, B., 2014. Plasticity-based modelling of fibre/matrix debonding in unidirectional composites. Composites and Structures **108**, 41–48.

Nedjar, B., Kotelnikova-Weiler, N., Stefanou, I., 2014. Modeling of unidirectional fibre-reinforced composites under fibre damage. Mechanics Research Communications **56**, 115–122.

Needleman, A., Borders, T., Brinson, L., Flores, V., Schadler, L., 2010. Effect of an interphase region on debonding of a CNT reinforced polymer composite. Composites Science and Technology **70**, 2207–2215.

Ochiai, S., Hojo, M., Inoue, T., 1999. Shear-lag simulation of the progress of interfacial debonding in unidirectional composites. Composites Science and Technology **59**, 77–88.

Ohno, N., Ando, T., Miyake, T., Biwa, S., 2002. A variational method for unidirectional fiber-reinforced composites with matrix creep. International Journal of Solids and Structures **39**, 159–174.

Perzyna, P., 1971. Thermodynamic theory of viscoplasticity. Advances in Applied Mechanics, vol. 11, Academic Press, New York.

Simo, J., Hughes, T., 1998. Computational inelasticity. Springer-Verlag, New York.

Spencer, A., 1984. Constitutive theory for strongly anisotropic solids, in: Spencer, A. (Ed.), Continuum theory of the mechanics of fibre-reinforced composites, CISM cources and lectures No. 282, Springer, Wien. pp. 1–32.

Weiss, J., Maker, B., Govindjee, S., 1996. Finite element implementation of incompressible, transversely isotropic hyperelasticity. Computer Methods in Applied Mechanics and Engineering **135**, 107–128.